Detection of the Intrinsic Size of Sagittarius A* Through Closure Amplitude Imaging

Geoffrey C. Bower,[1]* Heino Falcke,[2,3,4] Robeson M. Herrnstein,[5] Jun-Hui Zhao,[6] W. M. Goss,[7] Donald C. Backer[1]

We have detected the intrinsic size of Sagittarius A*, the Galactic center radio source associated with a supermassive black hole, showing that the short-wavelength radio emission arises from very near the event horizon of the black hole. Radio observations with the Very Long Baseline Array show that the source has a size of 24 ± 2 Schwarzschild radii at 7-millimeter wavelength. In one of eight 7-millimeter epochs, we also detected an increase in the intrinsic size of 60^{+25}_{-17}%. These observations place a lower limit to the mass density of Sagittarius A* of 1.4×10^4 solar masses per cubic astronomical unit.

Sagittarius A* (Sgr A*) is the compact, nonthermal radio source in the Galactic center associated with a compact mass of $4 \times 10^6\ M_\odot$ (*1–3*). It is the best-established and closest supermassive black hole candidate and serves as the prime test case for the black hole paradigm. Emission at radio, near-infrared (NIR), and x-ray wavelengths traces processes in the environment of the event horizon (*4–9*).

High-resolution radio imaging of Sgr A* can ultimately distinguish between the many different models for the emission, accretion, and outflow physics of the source as well as provide an important test of strong-field gravity (*10*). Sgr A* has been a target of such observations for the past 30 years (*11*). Its intrinsic size and structure have remained obscured, however, because radio waves from Sgr A* are scattered by turbulent interstellar plasma along the line of sight (*12*). The scatter-broadened image of Sgr A* is an ellipse, with the major axis oriented almost exactly east-west and a quadratic size-wavelength relation.

The turbulent plasma is parametrized with a power law of turbulent energy density as a function of length scale, with outer and inner scales that correspond to the scale on which turbulence is generated and damped, respectively. Scattering theory predicts that the scatter-broadened image will be a Gaussian when the inner length scale of the turbulent medium is larger than the longest baseline of the observing interferometer (*13*). Additionally, the scatter-broadened image size will scale quadratically as a function of wavelength. In the case of Sgr A*, the longest interferometer baseline used in our analysis, $b_{max} \sim 2000$ km, corresponds to a length scale in the scattering medium of $D_{scattering}/D_{source} \times b_{max} \sim 25$ km, where $D_{source} = 8$ kpc is the distance from Sgr A* to the Earth and $D_{scattering} = 100$ pc is the distance from Sgr A* to the scattering screen (*12*). This scale is much less than predicted and measured values of the inner scale, which fall in the range of 10^2 to $10^{5.5}$ km (*14*, *15*). The amplitude of turbulence in the Galactic center scattering screen is ~ 2 to 3 orders of magnitude greater than what is seen in the next most powerful scattering region, NGC 6334B (*16*), however, suggesting that the Galactic center case may be atypical.

The presence of strong scattering has pushed observations to shorter and shorter wavelengths where scattering effects decrease and intrinsic source structure may dominate, creating a deviation from the measured size-wavelength law. On the basis of extensive observations with the National Radio Astronomy Observatory (NRAO)'s Very Long Baseline Array (VLBA), L98 measures the index of the size-wavelength power law to be $\alpha = 1.99 \pm 0.03$ (*17*). L98 also claims a deviation from the scattering law in the minor axis at 7-mm wavelength (43 GHz), implying an intrinsic size of 72 Schwarzschild radii (R_s) (*18*).

Unfortunately, precise measurements of the size of Sgr A* are seriously hampered by calibration uncertainties related to the variable antenna gain and atmospheric opacity at the low antenna elevations necessary to observe Sgr A* from the Northern Hemisphere. Closure amplitudes have been used to constrain the size of Sgr A* with VLBI observations at 3.4 mm (*19*). The closure amplitude does not rely on calibration transfer from another source, as traditional imaging methods do, and is independent of all station-dependent amplitude errors. This method does not, however, eliminate baseline-dependent errors such as variable decorrelation (which also influence conventional calibration and imaging techniques). The closure amplitude is conceptually related to the closure phase, a more well-known quantity that is also independent of station-based gain errors. The principle drawback of closure amplitude analysis for simple source structures is the reduction in the number of degrees of freedom relative to a calibrated data set. The number of independent data points for a seven-station VLBA experiment is reduced by a factor of 14/21. Additionally, the closure amplitude method cannot determine the absolute flux density for the source. These shortcomings are more than offset by the confidence that the result gives through its accurate handling of amplitude calibration errors.

We describe here the analysis of new and archival VLBA data through closure amplitude and closure phase quantities. We analyze three new experiments including data at 1.3 cm, six new experiments including data at 0.69 cm, as well as 10 experiments from the VLBA archive including data at 6-, 3.6-, 2.0-, 1.3-, 0.77-, 0.69-, and 0.67-cm wavelengths.

Observations and initial data reduction. Six new observations were made with the VLBA as part of our Very Large Array flux density monitoring program (*20*). Three observations were made in each of two separate epochs in July and August 2001 and April and May 2002 (table S1). In the first epoch, observations at 1.3 cm and 0.69 cm were interleaved over 5 hours. In the second epoch, observations were obtained only at 0.69 cm in order to maximize the signal-to-noise ratio (SNR) of the final result. All observations were dual circular polarization with 256 Mbits s^{-1} recording rate.

We also analyzed a number of experiments from the VLBA archive over the wavelength range of 6.0 cm to 0.67 cm (table S1). The experiments BS055 A, B, and C were those analyzed by L98. The experiment BB113 was previously analyzed (*21*).

Initial data analysis was conducted with the NRAO Astronomical Imaging Processing System (AIPS) (*22*). Standard fringe-fitting techniques were used to remove atmospheric and instrumental delays from the data [Supporting Online Material (SOM) Text]. High SNR fringes were detected for most stations on the compact source NRAO 530 (J1733-1302), indicating the overall quality of the data. Because of the relatively larger size of Sgr A*, fringes were obtained for a subset of five to eight stations (table S1).

Data were then averaged over wavelength and time for each experiment. The quality of

[1]Astronomy Department and Radio Astronomy Laboratory, University of California, Berkeley, CA 94720, USA. [2]Radio Observatory Westerbork, ASTRON, Post Office Box 2, 7990 AA Dwingeloo, Netherlands. [3]Astronomy Department, University of Nijmegen, Postbus 9010, 6500 GL Nijmegen, Netherlands. [4]Max Planck Institut für Radioastronomie, Auf dem Hügel 69, D-53121 Bonn, Germany. [5]Department of Astronomy, Columbia University, Mail Code 5246, 550 West 120th Street, New York, NY 10027, USA. [6]Harvard-Smithsonian Center for Astrophysics, 60 Garden Street, MS 78, Cambridge, MA 02138, USA. [7]National Radio Astronomy Observatory, Array Operations Center, Post Office Box O, Socorro, NM 87801, USA.

*To whom correspondence should be addressed. E-mail: gbower@astro.berkeley.edu

the final result is dependent on the visibility averaging time. The longer the averaging time, the higher the SNR of the closure amplitude calculation (*23*). On the other hand, as the averaging time approaches the phase decorrelation time, the closure amplitudes cease to be accurate. It is not necessary, however, to determine the best averaging time precisely, because neither of these effects is a strong function of time (*23*). The results that we give are for an averaging time of 30 s, but we find that for averaging times of 15 to 120 s the estimated intrinsic size of Sgr A* does not differ by more than 10% (SOM Text). No amplitude calibration was applied at any stage. The averaged data were then written to text files for analysis by our own analysis programs, external to AIPS.

Closure amplitude and closure phase analysis of a single Gaussian. We formed the closure amplitude from the measured visibilities and averaged the closure amplitudes over time. Closure amplitudes were averaged over scans, which were 5 to 15 min in duration. The code uses the scatter in the closure amplitudes before averaging to determine the error in the closure amplitude. Only independent closure amplitudes were formed (*24*).

We selected visibility data only with station elevations $> 10°$ to reduce sensitivity to phase decorrelation, which is more substantial at low elevations. We also excluded data at (u, v) distances greater than 25 $M\lambda$ at 6.0 cm, 50 $M\lambda$ at 3.6 cm, 150 $M\lambda$ at 2.0 cm and 1.3 cm, and 250 $M\lambda$ at 0.69 cm where (u, v) are the coordinates of the Fourier transform of the sky brightness distribution, and λ is the wavelength. These sizes are comparable to the expected size of Sgr A* at each wavelength. Visibility amplitudes beyond the cutoff were indistinguishable by inspection from noise. This (u,v)-distance limit reduced sensitivity to the noise bias or station-dependent differences in the noise bias. Results were not strongly dependent on the value of this cutoff.

Model visibilities for each baseline and time datum were computed for an elliptical source of a given flux density S_0, major axis size x, minor axis size y, and position angle ϕ. In addition, a noise bias was added in quadrature to each model visibility. Our model visibility amplitude (squared) on baseline ij is then

$$A_{ij}^2 = S_0^2 e^{-D_0[(u'_{ij}x)^{\beta-2} + (v'_{ij}y)^{\beta-2}]} + N_{ij}^2 \quad (1)$$

where $D_0 = 2\left(\frac{\pi}{2\sqrt{log2}}\right)^2$, N_{ij} is the noise bias, and u_{ij}' and v_{ij}' are baseline lengths in units of wavelength in a coordinate system rotated to match the position angle ϕ. Model closure amplitudes were then formed from these model visibilities. We determine the best fit parameters with the use of a nonlinear fitting method that minimizes χ^2 between the model and measured closure amplitudes (fig. S1 and table S2). We find the reduced χ^2 for the amplitudes ${\chi_A}^2 \approx 1$ for all experiments.

In the case of an image produced by interstellar electron scattering on baselines longer than the inner scale of turbulence, β is the power law index of electron density fluctuations (*13*). The parameter β is related to the exponent α of the scattering law (size $\propto \lambda^\alpha$) as $\beta = \alpha + 2$, allowing an independent check of the λ^2 law (*13*–*15*). For the case of the Galactic center scattering, we expect $\beta = 4$, in which case Eq. 1 is a Gaussian function and x and y are the full widths at half maximum in the two axes. Allowing β to be unconstrained in our fits, we find $\beta = 4.00 \pm 0.03$, which is consistent with the expectation of scattering theory (fig. S3). All remaining analysis is conducted with the assumption that $\beta = 4$.

The introduction of the noise bias to the model changes our calculation from a pure closure amplitude to a noise-biased closure amplitude. We found that our results did not require that we consider the noise bias as dependent on station or time (SOM Text). Thus, we chose $N_{ij}(t) = N_0$ because it is simpler computationally and has a smaller number of independent parameters.

Errors in the model parameters were determined by calculating χ^2 for a grid of models surrounding the solution and fitting constant χ^2 surfaces (fig. S2). Monte Carlo simulations find confidence intervals that are smaller by a factor of 2 than those determined from the χ^2 analysis, suggesting that the dominant sources of error are baseline-based errors such as phase decorrelation, which were not included in the Monte Carlo simulations (SOM Text).

Closure phases were formed, averaged, and analyzed in a manner similar to the closure amplitudes. We tested the closure phases against the hypothesis that they are all zero. This hypothesis is the case for a single elliptical Gaussian and other axisymmetric structures with sufficiently smooth brightness distributions. An axisymmetric disk is a notable exception to this hypothesis because it induces ringing in the transform plane. The reduced χ^2 for this hypothesis is ${\chi_\phi}^2 \approx 1$ for all experiments (table S2), indicating no preference for multiple components, nonaxisymmetric structure, or disk-like structure.

Although the solutions for a single Gaussian component are sufficiently accurate, we did search the parameter space for two-component models. To do this, we performed a minimization of χ^2 with respect to closure amplitude and closure phase jointly. The reduced χ^2 for these models was roughly equal to the values for the single Gaussian component despite the addition of several degrees of freedom. We also calculated upper limits to the flux densities of secondary components that are in the range of 2 to 10%, typically (fig. S4 and table S2). The absence of any improvement indicates that a single Gaussian component is sufficient and the simplest model of the data. This absence is particularly important for the cases where $\chi^2 > 1$ and suggests, as noted before, that the results are dominated by closure errors rather than improperly modeled structure.

Scattering law and intrinsic size. We determined the size of the major and minor axes of Sgr A* for each experiment (Figs. 1 and 2 and table S2). The major axis is oriented almost exactly east-west. The major axis size is measured much more accurately than the minor axis size because of the poorer north-south resolution of the array. All major axis measurements at 1.3 and 0.69 cm are larger than the scattering size determined by L98 (*25*) and the scattering size that we determine below, although the difference is statistically significant in only one epoch at 0.69 cm. Minor axis measurements are distributed about the scattering result, and no one differs significantly from the expected result.

The L98 scattering law is adequate for the minor axis measurements as a function of wavelength (Fig. 3). All the measured minor axis sizes agree with the scattering law to better than 3σ. The data are also consistent with a constant position angle of $78.0^{+0.8}_{-1.0}$ with ${\chi_\nu}^2 = 2.2$ for $\nu = 6$ degrees of freedom.

We determine fits to the major and minor axis sizes as a function of wavelength with the use of subsets of the data with minimum wavelengths, λ_{min}, of 2.0 cm, 1.3 cm, 0.6 cm, and 0.3 cm (table S3). The last fit includes the 3.4-mm circular Gaussian fits for the major axis only (*19*). There are two fits for each subset, allowing α to vary and fixing α at 2. ${\chi_\nu}^2$ is less than 3 for the minor axis case with $\lambda \geq 0.6$ cm, confirming that the solution is adequate for $\alpha = 2$.

The major axis data, however, are discrepant from the L98 and the new scattering law (Fig. 3). All of the 7-mm results fall above the L98 scattering law. Two of these points are significantly different at greater than 3σ.

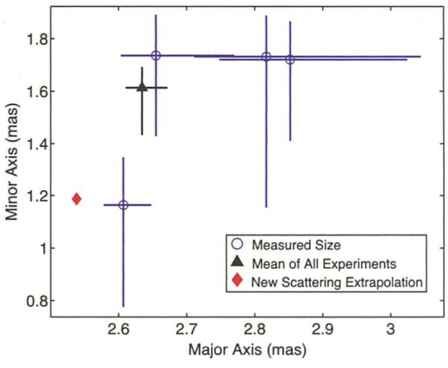

Fig. 1. Sizes from closure amplitude analysis of three new and one archival 1.3-cm VLBA experiments (open circles). The mean size (triangle) is significantly larger than the new scattering size (red diamond), which is a fit to all data at $\lambda \geq 2$ cm with $\alpha = 2$. mas, milli–arc sec.

The L98 scattering law predicts a size of 690 micro–arc sec at 0.69 cm, which is $\sim 7\sigma$ from the measured size (712^{+4}_{-3} micro–arc sec) and smaller than any of the measured sizes (Fig. 2). An attempt to fit a scattering law with $\alpha_{major} = 2$ to all data with $\lambda > 0.6$ cm gives $\chi_\nu^2 = 24$ for 6 degrees of freedom, demonstrating that the hypothesis can be strongly rejected. In fact, the 1.35-cm major axis size is also discrepant with the best fit $\alpha_{major} = 2$ scattering law, giving $\chi_\nu^2 = 5.6$ for 3 degrees of freedom.

We consider two alternative models for our results: case A, the scattering power law exponent α_{major} is not exactly 2, or case B, intrinsic structure in Sgr A* is distorting the size-wavelength relation at short wavelengths.

For case A, we find adequate solutions for all data at wavelengths ≥ 0.3 cm with $\alpha_{major} = 1.96 \pm 0.01$. The result is clearly discrepant with scattering theory, which requires $\beta = 4$, and marginally discrepant with our determination of the scattering theory parameter $\beta = 4.00 \pm 0.03$ (fig. S3), because scattering theory predicts that $\alpha = \beta - 2$.

For case B, we determine a new scattering law from observations with $\lambda \geq 2.0$ cm and $\alpha_{major} = 2$. This solution has a scale parameter σ^{1cm}_{major} that is even less than that of L98, increasing the discrepancy at short wavelengths. Removing this new scattering law in quadrature gives an intrinsic size of 700 ± 100 arc sec at 1.35 cm, 240 ± 10 arc sec at 0.69 cm and $60 \pm 50 \times 10^{-6}$ arc sec at 0.35 cm (Table 1). On the basis of the disagreement between β and α, we reject case A and claim that we have determined the size of intrinsic structure in Sgr A* at 1.35 and 0.69 cm.

The two cases predict substantially different sizes at 20 cm. For the major axis, case A predicts 541 ± 2 milli–arc sec, whereas case B predicts 595 ± 3. The 20.7-cm ($\nu = 1450$ MHz) major axis size of 624 ± 6 milli–arc sec measured with the VLA A array (*26*) is discrepant with both of these cases, although more strongly with case A. These measurements are particularly difficult because the source is only partially resolved in the A array: The synthesized beam is about 2.6×0.9 arc sec, oriented north-south. Additionally, extended structure in the Galactic center makes estimation of the size strongly dependent on the estimate of the zero-baseline flux density.

We attempted to verify the 20-cm size with analysis of three VLA A array observations at 21.6 cm obtained originally for polarimetry (*8*). Results for each of the three experiments were similar and dominated by systematic errors that make an estimate of the intrinsic size difficult. We were unsuccessful at analyzing these experiments with our closure amplitude technique, possibly because of the poor resolution of Sgr A* and inability of our code to handle the large number of stations. In any case, the reliability of amplitude calibration of the VLA at 20 cm reduces the need for closure amplitude analysis. We imaged all baselines and measured the total flux density of Sgr A* by fitting a two-dimensional Gaussian to the central 3″. For all epochs, we find an error in the total flux density of 10 mJy. We determined the size by fitting in the (u, v) plane with the total flux density fixed and with a minimum cutoff in (u, v) distance. For values of the total flux density that range from -1σ to $+1\sigma$ and for a minimum (u, v) distance from 20 to 120 $k\lambda$, we find that the major axis size varies systematically from 580×10^{-3} to 693×10^{-3} arc sec. The minor axis is very poorly constrained. We estimate the size from the mean of these results as $640 \times 10^{-3} \pm 40 \times 10^{-3}$ arc sec. We consider this to be a more reasonable estimate of the error in the size of Sgr A* than those previously given. This size is consistent at $< 1\sigma$ with case B and $\sim 1.5\sigma$ with case A, favoring slightly detection of the intrinsic size.

Although all minor axis data are adequately fit with $\alpha_{minor} = 2$, we can check the consistency of our results by estimating intrinsic sizes for this axis in the same way. The minor axis sizes show the same trend as the major axis sizes: smaller than the L98 scattering law at long wavelengths and larger than the L98 scattering law at short wavelengths (Fig. 3). With the use of the solution for $\alpha_{minor} = 2$ and $\lambda \geq 2.0$ cm, we estimate intrinsic sizes of $1.1 \times 10^{-3} \pm 0.3 \times 10^{-3}$ arc sec at 1.35 cm and $0.26 \times 10^{-3} \pm 0.06 \times 10^{-3}$ arc sec at 0.69 cm. These are comparable to the sizes determined for the major axis. For the case of unconstrained power law index fit to all data, we find $\alpha_{minor} = 1.85^{+0.06}_{-0.06}$, marginally consistent with no intrinsic source.

Changes in the source size with time. At 0.69 cm, the only measurement deviating significantly from the mean result is in the major axis for BB130B. The BB130B result is $700^{+30}_{-18} \times 10^{-6}$ arc sec, whereas the mean result is $712^{+4}_{-3} \times 10^{-6}$ arc sec, giving a difference of $58^{+30}_{-19} \times 10^{-6}$ arc sec. We note that the greatest deviation in the 0.69-cm position angle also occurs for BB130B, although the difference is significant only at the 2σ level. Any such deviation would indicate a nonsymmetric expansion or a nonsymmetric intrinsic source size. We can estimate the change in the size of the intrinsic source between BB130B and the mean size by subtracting in quadrature the case B scattering size from each. As stated above, the mean result implies an intrinsic size of $0.24 \times 10^{-3} \pm 0.01 \times 10^{-3}$ arc sec. The intrinsic size implied by the BB130B result is $0.38^{+0.06}_{-0.04} \times 10^{-3}$ arc sec. Thus, the growth in major axis size is $0.14^{+0.06}_{-0.04} \times 10^{-3}$ arc sec in the north-south direction. We cannot associate this change in structure with a flux density change. This maximum in the size comes $\sim$10 days before detection of an outburst at 0.69 cm with the VLA (*20*). The following

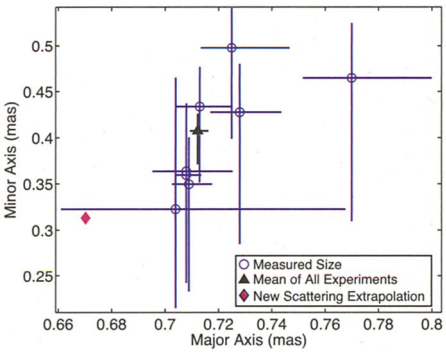

Fig. 2. Sizes from closure amplitude analysis of six new and two archival 0.69-cm VLBA experiments (open circles). The mean size (triangle) is significantly larger than the new scattering size (red diamond).

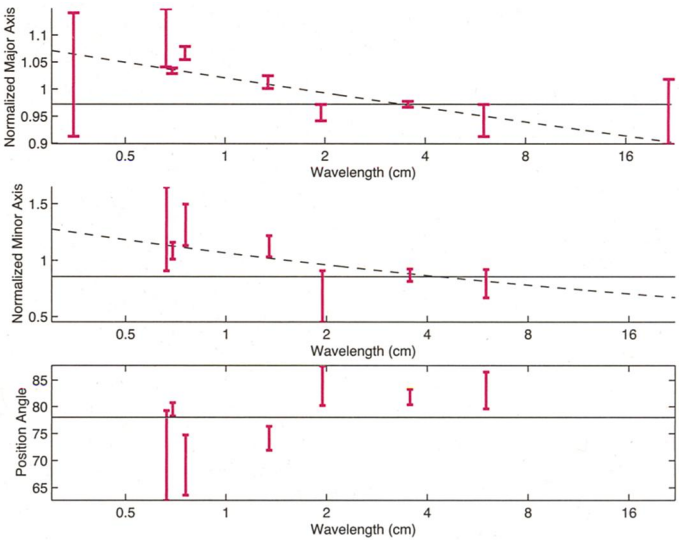

Fig. 3. Major axis size, minor axis size, and position angle as a function of wavelength normalized to the L98 scattering size. All results are determined by the closure amplitude technique except the 21.6-cm result, which is determined from conventional fitting. We also included a 3.5-mm measurement in the major axis (*19*). In the top two graphs, solid black lines show the best fit λ^2 scattering model for $\lambda \geq 2$ cm in the major and minor axis plots. The dotted lines show the best fit law with α unconstrained for $\lambda \geq 0.6$ cm. The black line in the bottom graph is our best fit value of 78° for the position angle.

epoch, BB130C, occurs only 2 days before this outburst but shows no deviation from the mean size, although the size is particularly poorly determined in this case.

The interstellar scattering screen. The image of a scattered source is created by turbulent plasma along the line of sight. The minimum time scale for the scattered image to change is the refractive time scale, the time in which the relative motions of the observer, turbulent plasma, and background source lead to the background source being viewed through a completely different region of the interstellar plasma. The refractive time scale for Sgr A* is $\sim 0.5\ \lambda^2$ year cm^{-2}, given a relative velocity of 100 km s^{-1} (*13*). At our longest wavelength for VLBA observations, 6 cm, the time scale is 20 years. At our shortest wavelength of 7 mm, the time scale for refractive changes is 3 months. Our observations are distributed over a much larger time frame than 3 months, implying that the mean result may be affected by refractive changes.

Two subsets of the archival data have much smaller spans, however. The BS055 experiments cover 6.0 to 0.69 cm in 1 week and the BL070 and BB113 experiments cover 6.0 cm to 0.67 cm in 3 months. These data sets include all of the 2.0-cm and longer wavelength data. If we compare the 0.7-cm size, we see that it is larger in these quasi-simultaneous experiments than that of the mean of all experiments and also larger than the expectation of the new scattering law. We find 0.69-cm major axis sizes of $728^{+16}_{-11} \times 10^{-6}$ arc sec and $713^{+12}_{-9} \times 10^{-6}$ arc sec for BS055C and BL070B, respectively, both larger than the mean size of $712^{+4}_{-3} \times 10^{-6}$ arc sec (table S2). We conclude that, if refractive effects are altering the short wavelength results, then their effect is to reduce the deviation from the scattering law, not enhance it.

Discussion. Our results allow us to probe the mechanisms responsible for accretion, outflow, and emission in the vicinity of the black hole. We can compare the measured 7-mm intrinsic major axis size of 24 R_s and its dependence on wavelength with expected values (Fig. 4). The intrinsic size of the major axis decreases with wavelength and is best fit with a power law as a function of wavelength, with index $\alpha_{intrinsic} = 1.6 \pm 0.2$. We find for the minor axis a similar value, $\alpha_{intrinsic} = 2.1 \pm 0.5$. With the assumption that the source is circularly symmetric and the use of the mean flux density of 1.0 J year at 7 mm (*20*), we compute a brightness temperature of $T_b = 1.2 \times 10^{10} \times \left(\frac{\lambda}{0.7\ \text{cm}}\right)^{-1.2}$ K. This result is a lower limit, because the source may be smaller in the minor axis. A brightness temperature in excess of 10^{10} K is a strong indication that synchrotron radiation is the dominant emission mechanism at work.

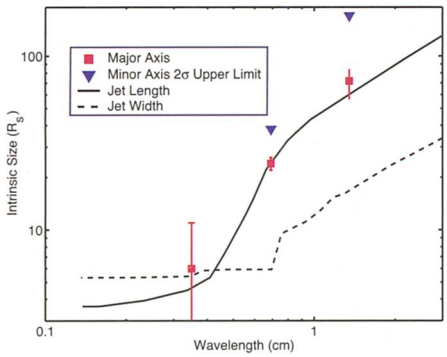

Fig. 4. The intrinsic size of Sgr A* as a function of wavelength. We plot the best fit size in the major axis and 2σ upper limits to the size of the minor axis. We also plot one set of predictions for jet length and jet width (*29*).

The wavelength-dependent size of Sgr A* now unambiguously shows that the source is stratified because of optical depth effects. We rule out models in which the emission originates from one or two zones with simple monoenergetic electron distributions (*27*). These models predict a size that is constant with wavelength and is larger than our measured size.

The results are well fit by a multizone or inhomogeneous model, in which the size is equal to the radius at which the optical depth is equal to unity (*28*). In a jet model, declining magnetic field strength, electron density, and electron energy density contribute to a size that becomes smaller with wavelength. A detailed jet model for Sgr A* predicts an intrinsic size of 0.25×10^{-3} arc sec at 0.69 cm and 0.6×10^{-3} arc sec at 1.3 cm (Fig. 4) (*29*). Exact values and wavelength dependence are a function of a number of parameters, including the relative contributions of the extended jet and the compact nozzle component of the jet. The jet model also predicts that the source should be elongated, with an axial ratio of 4:1. The apparent measured symmetry in the deconvolved sizes in each axis, however, does not imply that the intrinsic source is symmetric. For example, an elongated intrinsic source that is oriented at 45° to the scattering axis will produce equal deconvolved sizes in each axis. Modeling of the closure amplitudes with a complete source and scattering model is necessary to determine the elongation for the most general case.

The thermal, high accretion rate models such as Bondi-Hoyle accretion (*30*) and advection dominated accretion flows (*31*) require $T_b \lesssim 10^9$ K, which overpredicts the size in each axis by a factor of 3. This disagreement confirms the elimination of these models on the basis of the polarization properties of Sgr A* (*9*). On the other hand, the radiatively inefficient accretion flow (RIAF) model (*32*) has a lower accretion rate and higher T_b, compatible with the polarization and with this measurement. The RIAF model also predicts an inhomogeneous electron distribution consistent with a size that reduces with decreasing wavelength. Both the RIAF model and the jet model are similar in the electron energy distribution and magnetic field distribution required to produce the observed flux density within the observed size. These models differ principally in the relative contribution of thermal electrons to emission in the submillimeter region of the spectrum.

Table 1. Intrinsic size of the major axis of Sgr A*. Measured and scattering sizes are micro–arc sec.

Wavelength (cm)	Measured size	Scattering size	Intrinsic size (R_s)
1.35	2635^{+37}_{-24}	2533^{+20}_{-20}	72^{+15}_{-11}
0.69	712^{+4}_{-3}	669^{+5}_{-5}	24^{+2}_{-2}
0.35	180^{+20}_{-20}	173^{+2}_{-2}	6^{+5}_{-5}

Extrapolating our size-wavelength relation to longer wavelengths, we estimate a size at 2 cm of 130 R_s, with a characteristic light travel time of 85 min. This is comparable to the shortest time scale for radio variability detected, 2 hours, during which the 2.0 cm radio flux density changed by 20% (*8*). The smooth nature of the spectrum from 90 cm to 7 mm suggests that our size-wavelength relation holds over that entire range (*33*).

Our relation implies a size $< 2R_s$ at 1.3 mm, comparable to the size of the event horizon. The decrease of the source size with wavelength cannot continue much farther because of the finite size of the central object itself. In the millimeter and submillimeter, however, the spectral index rises (*34*), indicating that there may be a break in the size-wavelength relation. Ultimately, the size of the event horizon can be viewed as setting a limit on the wavelength of the peak emission. The strong break in the spectrum between the submillimeter and the NIR may correspond to the wavelength at which the source size becomes comparable to the event horizon. Even with a weaker dependence of size on wavelength, the light travel time scale at millimeter wavelengths is a few minutes, comparable to the shortest time scale observed at x-ray and NIR wavelengths. This coincidence suggests that the bright flares observed at higher energies (*5*–*7*) are related to the submillimeter part of the spectrum and come from the vicinity of the black hole. The proximity of the millimeter emission indicates that emission at this and shorter wavelengths will be subject to strong light-bending effects, providing a unique probe of strong-field general relativity (*10*, *35*).

The size-wavelength relation also implies that the black hole mass must be contained within only a few Schwarzschild radii. Radio proper motion measurements require that Sgr A* must contain a significant fraction, if not all, of the compact dark mass found in the Galactic center (*36*–*38*). With the use of only our 7-mm size and the lower limit of the Sgr A* mass of $4 \times 10^5\ M_\odot$, we conservatively find that the mass density in Sgr A* has to be

strictly above 1.4×10^4 $M_\odot$ AU^{-3}. The dynamical lifetime of a cluster of objects with that density would be less than 1000 years, making Sgr A* the most convincing existing case for a massive black hole (*39*).

References and Notes

1. F. Melia, H. Falcke, *Annu. Rev. Astron. Astrophys.* **39**, 309 (2001).
2. A. M. Ghez *et al.*, *Astrophys. J.* **586**, 127L (2003).
3. R. Schödel *et al.*, *Astrophys. J.* **596**, 1015 (2003).
4. H. Falcke *et al.*, *Astrophys. J.* **499**, 731 (1998).
5. R. Genzel *et al.*, *Nature* **425**, 934 (2003).
6. A. M. Ghez *et al.*, *Astrophys. J.* **601**, 159L (2004).
7. F. K. Baganoff *et al.*, *Nature* **413**, 45 (2001).
8. G. C. Bower, H. Falcke, R. J. Sault, D. C. Backer, *Astrophys. J.* **571**, 843 (2002).
9. G. C. Bower, M. C. H. Wright, H. Falcke, D. C. Backer, *Astrophys. J.* **588**, 331 (2003).
10. H. Falcke, F. Melia, E. Agol, *Astrophys. J.* **528**, 13L (2000).
11. W. Goss, R. Brown, K. Lo, *Astron. Nachr.* **324** (suppl.), 497 (2003).
12. T. J. W. Lazio, J. M. Cordes, *Astrophys. J.* **505**, 715 (1998).
13. R. Narayan, J. Goodman, *Mon. Not. R. Astron. Soc.* **238**, 963 (1989).
14. P. N. Wilkinson, R. Narayan, R. E. Spencer, *Mon. Not. R. Astron. Soc.* **269**, 67 (1994).
15. K. M. Desai, A. L. Fey, *Astrophys. J. Supp. Ser.* **133**, 395 (2001).
16. A. S. Trotter, J. M. Moran, L. F. Rodriguez, *Astrophys. J.* **493**, 666 (1998).
17. K. Y. Lo, Z. Q. Shen, J. H. Zhao, P. T. P. Ho, *Astrophys. J.* **508**, 61L (1998).
18. We assume for Sgr A* a black hole mass of 4×10^6 $M_\odot$ and a distance of 8.0 kpc (*2*). The latter implies that 0.1 milli–arc sec = 0.8 AU = 1.1×10^{13} cm. Together, these quantities imply a Schwarzschild radius $R_s = 2GM/c^2 = 1.2 \times 10^{12}$ cm = 0.08 AU = 0.01 milli–arc sec, where G is Newton's gravitational constant.
19. S. S. Doeleman *et al.*, *Astron. J.* **121**, 2610 (2001).
20. R. Herrnstein, J.-H. Zhao, G. C. Bower, W. M. Goss, *Astron. J.*, in press.
21. G. C. Bower, D. C. Backer, R. A. Sramek, *Astrophys. J.* **558**, 127 (2001).
22. E. W. Greisen, *Information Handling in Astronomy: Historical Vistas* (Kluwer Academic Publishers, Dordrecht, Netherlands, 2003), pp. 109–126.
23. A. E. E. Rogers, S. S. Doeleman, J. M. Moran, *Astron. J.* **109**, 1391 (1995).
24. A. R. Thompson, J. M. Moran, G. W. Swenson, *Interferometry and Synthesis in Radio Astronomy* (Wiley, New York, 2001).
25. L98 determined a scattering law $\sigma_{axis} = \sigma^{1cm}_{axis}\,\lambda^{\alpha}_{axis}$, where axis is either major or minor, λ is given in cm, $\sigma^{1cm}_{major} = 1.43 \pm 0.02$ milli–arc sec, and $\sigma^{1cm}_{minor} = 0.76 \pm 0.05$ milli–arc sec. α is the index of the scattering law and it is assumed to be 2 for the strong scattering case. L98 found $\alpha_{major} = 1.99 \pm 0.03$. The major axis is oriented almost purely east-west at a position angle of 80° east of north.
26. F. Yusef-Zadeh, W. Cotton, M. Wardle, F. Melia, D. A. Roberts, *Astrophys. J.* **434**, 63L (1994).
27. T. Beckert, W. J. Duschl, *Astron. Astrophys.* **328**, 95 (1997).
28. R. D. Blandford, A. Konigl, *Astrophys. J.* **232**, 34 (1979).
29. H. Falcke, S. Markoff, *Astron. Astrophys.* **362**, 113 (2000).
30. F. Melia, *Astrophys. J.* **426**, 577 (1994).
31. R. Narayan, R. Mahadevan, J. E. Grindlay, R. G. Popham, C. Gammie, *Astrophys. J.* **492**, 554 (1998).
32. F. Yuan, E. Quataert, R. Narayan, *Astrophys. J.* **598**, 301 (2003).
33. M. E. Nord, T. J. W. Lazio, N. E. Kassim, W. M. Goss, N. Duric, *Astrophys. J.* **601**, 51L (2004).
34. J. Zhao *et al.*, *Astrophys. J.* **586**, L29 (2003).
35. A. Broderick, R. Blandford, *Mon. Not. R. Astron. Soc.* **342**, 1280 (2003).
36. D. C. Backer, R. A. Sramek, *Astrophys. J.* **524**, 805 (1999).
37. M. J. Reid, A. C. S. Readhead, R. C. Vermeulen, R. N. Treuhaft, *Astrophys. J.* **524**, 816 (1999).
38. M. Reid *et al.*, *Astron. Nachr.* **324**, S1 (2003).
39. E. Maoz, *Astrophys. J.* **494**, 181L (1998).
40. The National Radio Astronomy Observatory is a facility of NSF, operated under cooperative agreement by Associated Universities, Incorporated.

Supporting Online Material

www.sciencemag.org/cgi/content/full/1094023/DC1
SOM Text
Figs. S1 to S4
Tables S1 to S3
References

25 November 2003; accepted 22 March 2004
Published online 1 April 2004;
10.1126/science.1094023
Include this information when citing this paper.

REPORTS

In-Plane Spectral Weight Shift of Charge Carriers in $YBa_2Cu_3O_{6.9}$

A. V. Boris,* N. N. Kovaleva,† O. V. Dolgov, T. Holden,‡ C. T. Lin, B. Keimer, C. Bernhard

The temperature-dependent redistribution of the spectral weight of the CuO_2 plane–derived conduction band of the $YBa_2Cu_3O_{6.9}$ high-temperature superconductor (superconducting transition temperature = 92.7 kelvin) was studied with wide-band (0.01– to 5.6–electron volt) spectroscopic ellipsometry. A superconductivity-induced transfer of the spectral weight involving a high-energy scale in excess of 1 electron volt was observed. Correspondingly, the charge carrier spectral weight was shown to decrease in the superconducting state. The ellipsometric data also provide detailed information about the evolution of the optical self-energy in the normal and superconducting states.

The mechanism of high-temperature superconductivity (HTSC) is one of the main unsolved problems in condensed-matter physics. An influential class of theories predicts that HTSC arises from an unconventional pairing mechanism driven by a reduction of the kinetic energy of the charge carriers in the superconducting (SC) state (*1–3*). This contrasts with the conventional Bardeen-Cooper-Schrieffer (BCS) model, where correlations of the charge carriers below the SC transition temperature, T_c, bring about an increase in their kinetic energy (*4*, *5*), which is overcompensated for by a reduction of the potential energy due to the phonon-mediated attraction. Within a nearest-neighbor tight-binding model, measurements of the optical conductivity $\sigma_1(\omega) = Re[\sigma(\omega)]$ can provide experimental access to the kinetic energy $\langle K \rangle$ via the sum rule for the spectral weight $SW(\tilde{\Omega}) = \int_0^{\tilde{\Omega}} \sigma_1(\omega) d\omega = \frac{\pi e^2 a^2}{2\hbar^2 V_u} \langle -K \rangle$, where a is the in-plane lattice constant and V_u is the unit cell volume (*3*, *6–8*). The upper integration limit, $\tilde{\Omega}$, needs to be high enough to include all transitions within the conduction band but sufficiently low to exclude the interband transitions.

Precise optical data may thus enable one to address the issue of a kinetic energy–driven HTSC pairing mechanism. In fact, optical measurements have ruled out a lowering of the kinetic energy along the c axis (perpendicular to the highly conducting CuO_2 planes) as the sole mechanism of HTSC (*9*), but have also shown that it can contribute significantly to the superconducting condensation energy of multilayer copper oxides (*10*, *11*). Recently, experimental evidence for an alternative mechanism driven by a reduction of the in-plane kinetic energy (*3*) has been reported (*12*, *13*). The comprehensive data set presented here, however, demonstrates that this scenario is not viable.

We performed direct ellipsometric measurements of the complex dielectric function $\varepsilon(\omega) = \varepsilon_1(\omega) + i\varepsilon_2(\omega) = 1+$

Max-Planck-Institut für Festkörperforschung, Heisenbergstrasse 1, D-70569 Stuttgart, Germany.

*To whom correspondence should be addressed. E-mail: A.Boris@fkf.mpg.de

†Also at the Institute of Solid State Physics, Russian Academy of Sciences, Chernogolovka, Moscow district, 142432 Russia.

‡Present address: Department of Physics, Brooklyn College of the City University of New York, Brooklyn, NY 11210, USA.